

Networking of shear zones at the brittle-to-viscous transition (Cap de Creus, NE Spain)

F. Fousseis^{a,*}, M.R. Handy^a, C. Schrank^b

^a Department of Geology, Freie Universität Berlin, Germany

^b Department of Geology, University of Toronto, Canada

Received 10 August 2005; received in revised form 7 March 2006; accepted 9 March 2006

Available online 8 May 2006

Abstract

A crustal-scale shear zone network at the fossil brittle-to-viscous transition exposed at Cap de Creus, NE Spain evolved by coeval fracturing and viscous, mylonitic overprinting of an existing foliation. Initial fracturing led to mylonitic shearing as rock softened in ductilely deformed zones surrounding the fractures. Mylonitic shear zones widened by lateral branching of fractures from these shear zones and by synthetic rotation of the existing foliation between the fractures and shear zones. Shear zones lengthened by a combination of fracturing and mylonitic shearing in front of the shear zone tips. Shear zones interconnected along and across their shearing planes, separating rhomb-shaped lozenges of less deformed rock. Lozenges were subsequently incorporated into the mylonitic shear zones by widening in the manner described above. In this way, deformation became homogeneous on the scale of initial fracturing (metre- to decametre-scale). In contrast, the shear zone network represents localisation of strain on a decametre-length scale. The strength of the continental crust at the time of coeval fracturing and viscous shearing is inferred to have decreased with time and strain, as fracturing evolved to mylonitic shearing, and as the shear zones coalesced to form a through-going network subparallel to the shearing plane. Crustal strength must therefore be considered as strain- and scale-dependent.

© 2006 Elsevier Ltd. All rights reserved.

Keywords: Brittle-to-viscous transition; Mylonite; Shear zone; Crustal rheology; Faulting

1. Introduction

Crustal-scale *shear zones* are interpreted to transect the lithosphere, extending from the brittle upper crust through the transition to viscous, mylonitic flow in the middle crust down to the viscously deforming lower crust or upper mantle (e.g. Gilbert et al., 1994; Thatcher and England, 1998). Exhumed, ancient segments of this transition, here termed the brittle-to-viscous transition (BVT), usually consist of a system of networked shear zones (Mitra, 1979; Choukroune and Gapais, 1983; Hobbs et al., 1986; Gapais et al., 1987) in which brittle and viscous deformation are mutually overprinting (e.g. Passchier, 1984; Hobbs et al., 1986).

Knowledge of the temporal and kinematic evolution of *shear zone networks* at the BVT is crucial for understanding the evolution of crustal rheology at the BVT. Due to the broadly coeval activity of brittle and viscous deformation mechanisms, this rheology is expected to be sensitive to several parameters,

primarily effective pressure, temperature and strain rate (e.g. Sibson, 1980; Hobbs et al., 1986; Handy et al., in press).

Shear zone networks (SZNs) have been studied in nature (e.g. Mitra, 1979; Bell, 1981; Choukroune and Gapais, 1983; Gapais et al., 1987; Lafrance et al., 1998; Stewart et al., 2000; Carreras, 2001; Imber et al., 2001; Arbaret and Burg, 2003), as well as in experiments (e.g. Cobbold et al., 1971; Harris and Cobbold, 1985; Dennis and Secor, 1987; Williams and Price, 1990; Herwegh and Handy, 1996; Huddleston, 1999), with most work devoted to the kinematics of strain partitioning in a system of networked shear zones. Other contributions deal with theoretical aspects of rheology as well as the dynamics of SZNs (Handy, 1994; Regenauer-Lieb and Yuen, 2003), but little is known about how shear zones actually network (Arbaret and Burg, 2003).

The mylonite belt at the Cap de Creus, northeastern Spain (Fig. 1a), allows insight into the evolution of a crustal-scale shear zone network that formed in quartz-rich metasedimentary rocks under greenschist-facies conditions at the BVT. Available age constraints indicate that the mylonite belt probably formed during the late stages of the Variscan orogeny (Druguet, 2001). Carreras (2001) proposed nucleation models that apply to most of the large-scale folds, shear zones and shear zone networks in the Cap de Creus mylonite belt. In this

* Corresponding author. Tel.: +49 3083 870339; Fax: +49 3083 870734.
E-mail address: fousseis@zedat.fu-berlin.de (F. Fousseis).

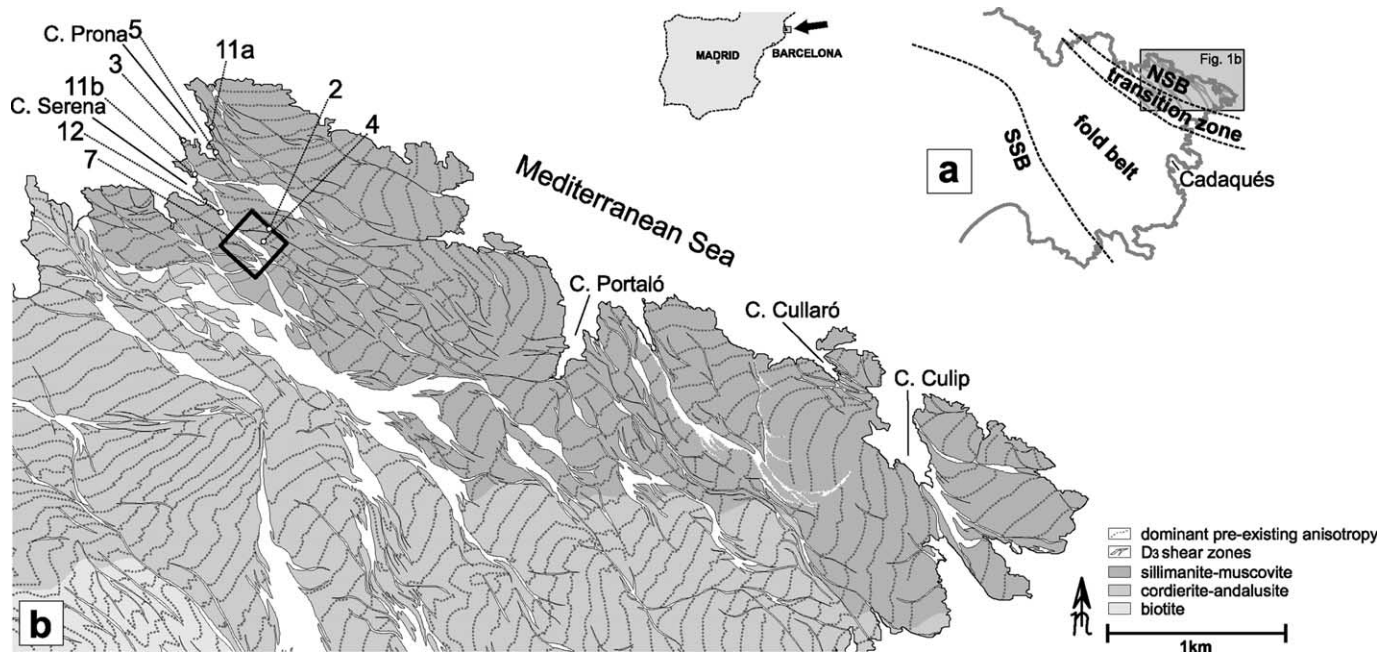


Fig. 1. Close-up of the northern Cap de Creus peninsula: (a) schematic map of the deformation at the Cap de Creus. SSB—Southern Shear Belt, NSB—Northern Shear Belt, from Carreras (2001); (b) structural map of the northern Cap de Creus peninsula showing the metamorphic zonation, the principal trends of the dominant $S_{1/2}$ foliation (dotted line is a composite of $S_{0/1}$ and $S_{1/2}$) and the D_3 shear zones forming the ‘Northern Shear Belt’. Insets mark the locations of figures below. Modified from Carreras (2001) and Druguet (2001).

paper, we present a complementary model for the evolution of those parts of the Cap de Creus mylonite belt where the close spatial and temporal association of brittle fracturing and viscous, mylonitic shearing cannot be explained by these previously published models.

It will be shown that shear zones originated as shear fractures before coalescing to form a network of mylonitic shear zones. Once networked, the shear zones widened by a combination of fracturing and mylonitic shearing. Initially heterogeneous and highly localised strain was transformed into a system of decametre-wide shear zones. Deformation became homogenised on the initial scale of fracturing, while becoming heterogeneous on a larger length scale. Specialised structural terms used in the text are defined in Appendix A and are printed in *italics* where they appear in the text for the first time.

2. Geological setting

The protolith rocks of the shear belt at the Cap de Creus peninsula are late Precambrian or Cambro-Ordovician age metasediments (Druguet and Hutton, 1998) consisting of mostly psammitic and pelitic layers. During the Variscan orogeny, these sediments experienced a low-pressure, greenschist- to amphibolite-facies metamorphism, which increases in grade from SW to NE on a much longer length scale than the investigated shear zones (Fig. 1b; Druguet, 2001). At least three deformational events can be discerned during this metamorphism:

1. S_1 developed parallel to bedding, S_0 , prior to the peak of metamorphism, yielding a composite foliation, $S_{0/1}$. This

D_1 deformation involved boudinage and isoclinal F_1 folding of quartz segregations.

2. During D_2 the composite $S_{0/1}$ was folded and sheared under peak, amphibolite-facies conditions, leading to the formation of a composite $S_{1/2}$ in the E–W-trending limbs of tight to isoclinal F_2 folds (e.g. in the Cala Serena and Cala Prona areas in Fig. 1; see also Carreras et al., 2005). The amplitudes of these folds vary from centimetre to metre scales depending on the initial thickness of the sedimentary layers. Fold limbs are strongly thinned (Fig. 2). The D_2 shear plane was oriented ESE–WNW and shearing on the kilometre-scale involved dextral, non-coaxial flow (Druguet et al., 1997; Bons et al., 2004). Locally, melt-bearing layers developed synchronously with S_2 (Druguet and Hutton, 1998), whereas granitoids and pegmatites intruded prior to or during D_2 (Druguet, 2001; Bons et al., 2004).
3. D_3 deformation is marked by several structural domains in the northern part of the Cap de Creus peninsula (Fig. 1), described here in order of increasing strain intensity: in the southwest, open to close F_3 folds without shear zones (‘fold belt’ in Fig. 1a) are gradational to the northeast to a domain of asymmetrical F_3 folding (cf. Fig. 12 in Carreras, 2001). Further to the NE, these folds have sheared limbs and fold axes parallel to L_3 stretching lineations (defined by aligned quartz and feldspar) and are transitional to retrograde, greenschist-facies shear zones that crosscut all pre-existing fabrics (‘transition zone’ of Carreras and Casas (1987) and Carreras (2001)). In the northeastern-most part of the Cap de Creus peninsula, these shear zones become interconnected to form the ‘Northern Shear Belt’



Fig. 2. Photograph of D_2 folds and associated $S_{1/2}$ composite foliation in the host rock for the D_3 shear zones. Note the thinned layers of $S_{0/1}$ in the sheared fold limbs forming $S_{1/2}$ (arrows 1 and 2). D_2 folding generally varies in intensity. Folds may be more symmetric than shown in this picture (see foliation trajectories in Fig. 5). Photograph was taken looking towards the N, hand lens for scale. UTM 31T 522017 east, 4686974 north.

(Carreras and Casas, 1987). Their kinematics reflect right-lateral transpressive shearing (Carreras, 2001).

In the northernmost Cap de Creus, D_3 began at around 560 °C and 2.4 Kbar (Druguet, 2001), conditions that are corroborated by the dynamic recrystallization of feldspars in pegmatite (e.g. Tullis and Yund, 1991). Quartz in D_3 mylonites recrystallised by subgrain rotation and grain boundary bulging, indicating syndeformational temperatures of 450 ± 50 °C at assumed strain rates of 10^{-11} – 10^{-10} s $^{-1}$ (Stipp et al., 2002; Fousseis and Handy, 2006). No signs of static recrystallisation were found in D_3 mylonites. D_3 was therefore active in a temperature interval corresponding to upper- to sub-green-schist facies conditions.

Our investigation focussed on selected parts of the ‘Northern Shear Belt’. This shear belt typically consists of two sets of shear zones (Fig. 1b): (1) NW–SE-trending, shallowly NE-dipping shear zones that accommodated top-SE shear parallel to moderately NW-plunging stretching lineations; (2) interlinking E–W-trending, northward-dipping shear zones with more steeply NW-plunging stretching lineations. The latter either accommodated oblique thrusting towards the SE or oblique-slip, down-dip movement towards the NW. As shown below, these movements all occurred within a common kinematic framework and the observations described below indicate that differently oriented shear zones interacted to accommodate deformation compatibly on the kilometric scale of the entire shear belt.

3. Nucleation and growth of shear zone networks at the BVT

The nucleation, growth and networking of shear zones are best exposed in the Cala Serena and Cala Prona areas, along the

northern shore of the Cap de Creus peninsula (Fig. 1b). By tracing these shear zones across and along their strike, we were able to establish a preserved sequence of three evolutionary stages. This space-for-time substitution is based on the premise that all the shear zones developed during one continuous tectonometamorphic phase (D_3), an assumption that is supported by our observations described below.

3.1. Strain localisation within fractures

Over the entire area, mylonitic shear zones are associated with fractures that occur either individually parallel to the overall D_3 shear plane (trending NW–SE and dipping to the NE, Figs. 3 and 4) or emerge from the tips and margins of mylonitic shear zones (arrows 4–6 in Figs. 5a and 11). Both kinds of fracture never crosscut D_3 mylonites and displacement along them is consistent with the overall dextral shear sense of the D_3 shear zones (Figs. 3 and 4).

Individual fractures range in length from a few centimetres to about 3 m. Longer fractures up to 10 m in length consist of several interconnected fracture segments (Figs. 3 and 4). Where no mylonitic shear zones formed, the rock contains fractures up to several metres in length with no slip and no signs of a ductile damage zone around them.

Faults show warped $S_{1/2}$ surfaces that form a monocline beyond their tips. These monoclines correspond to the ‘ductile beads’ described by Elliott (1976) (arrows in Figs. 3 and 4). The $S_{1/2}$ surfaces along the faults show a normal drag, with sharp cut-offs where they intersect the fracture plane. The normal sense of drag is consistent with the movement inferred from monoclinical folding of $S_{1/2}$ in the ductile bead (arrows in Figs. 3 and 4).

Fault tips often splay anticlockwise from the shearing plane to become parallel to $S_{1/2}$ away from the fractures (arrows 1

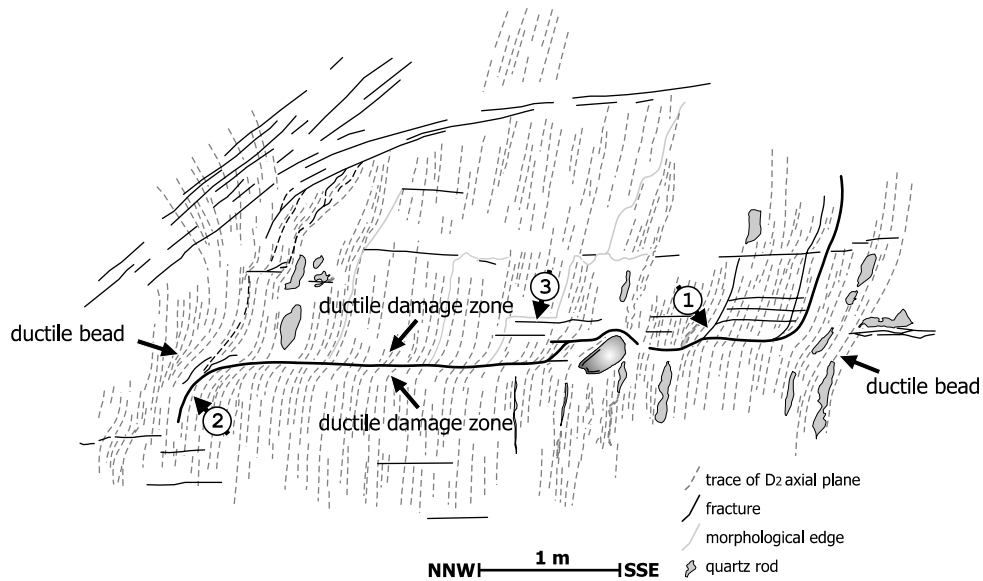


Fig. 3. Sketch map of a shear fracture at the northernmost tip of the peninsula separating Cala Serena from Cala Prona. Note bending of $S_{1/2}$ marking the ductile bead, as well as the fault drag along the fracture. See text for explanation. UTM 31T 521586 east, 4687501 north.

and 2 in Fig. 3). These splays are more pronounced in metapsammities than in metapelites. Modes of fracturing and sense of shear along these tip fracture segments could not be determined macroscopically. In a few cases, fault tips curve clockwise into a high-angle orientation with respect to $S_{1/2}$. Anticlockwise splays probably reflect the influence of $S_{1/2}$ (Ivins et al., 1990; Ranalli and Yin, 1990; Yin and Ranalli, 1992) as well as of changed principal stress orientations at fault tips (e.g. Vermilye and Scholz, 1999) on propagating fractures. In contrast, clockwise curving fault tips resemble fault terminations in homogeneous rocks (horse-tail splays, e.g. Kim et al., 2004).

Existing lithological variations (a 100 μm –2-mm-spaced foliation on the microscopic scale and a 20–200-cm-thick layering on the outcrop scale; Fig. 5b) influence fracture propagation. On the microscopic scale, fractures are usually deflected by mica-rich $S_{1/2}$ cleavage domains, where they tend to form shear bands, whereas Qtz- and Fsp-dominated microlithons are cross-cut obliquely by narrow fractures (Fousseis and Handy, 2006). On the outcrop scale, faults and also mylonitic shear zones that crosscut metapelitic layers show relatively narrow drags. Besides these, however, no systematic variations of style, orientation or spacing were found that might have been caused by the different lithologic variations.

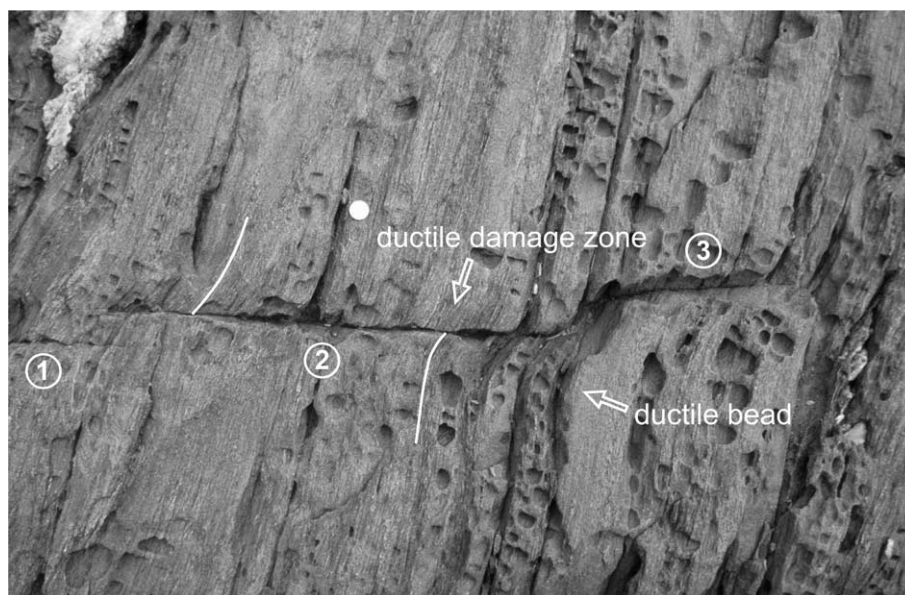


Fig. 4. Three, longitudinally linked, shear fractures (labelled 1–3) on the eastern slope of southern Cala Serena. Note the flexure of $S_{1/2}$ forming a ductile bead beyond the fracture tips and the drags with the sharp cut-offs along the central fracture (white lines). Note that white lines illustrate dragging of $S_{1/2}$ and do not denote a marker. Photograph is taken looking towards the E, diameter of coin is 2.3 cm. UTM 31T 521959 east, 4686946 north.

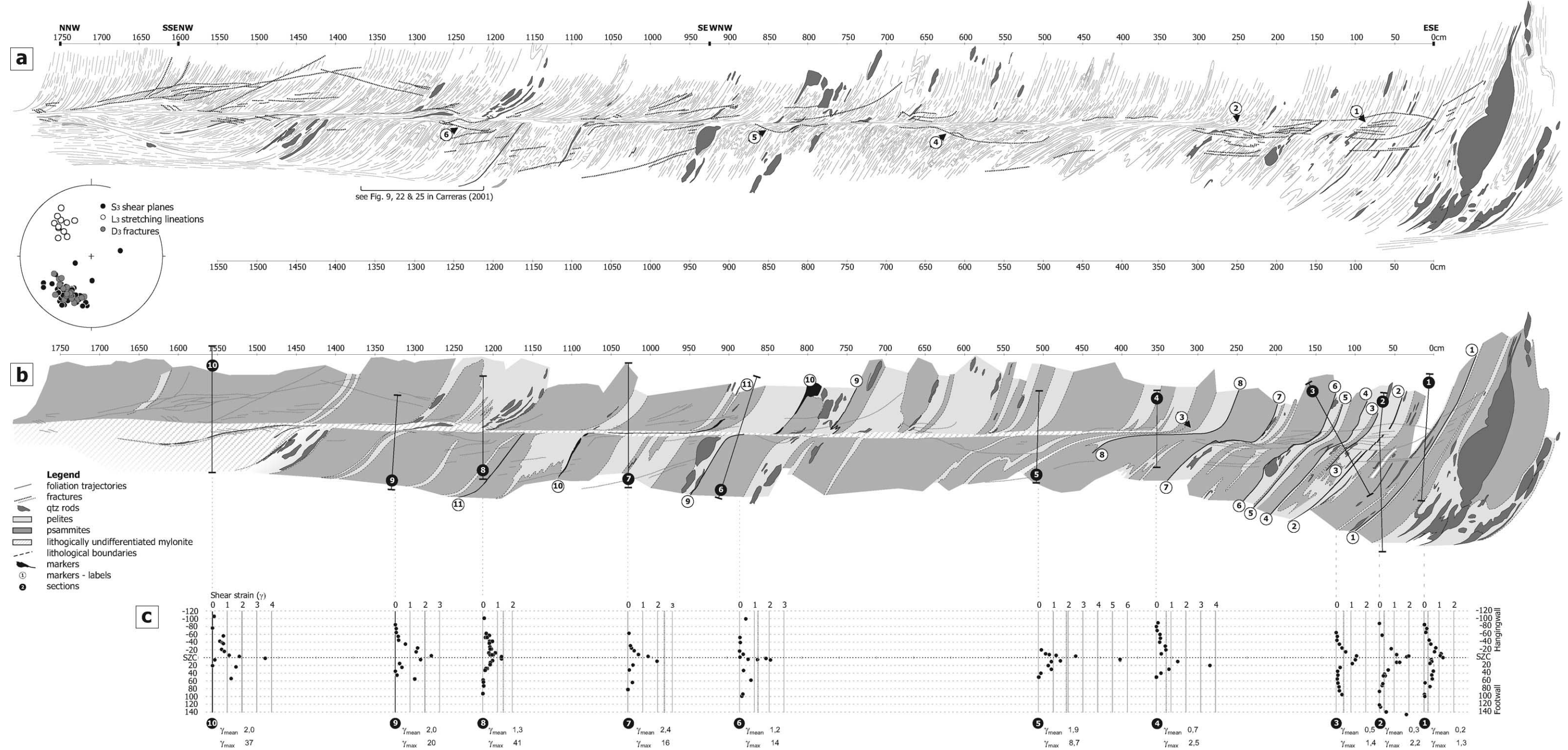


Fig. 5. Shear zone termination in the Cala Prona (cf. fig. 21 in Carreras, 2001): (a) sketch map shows foliation trajectories, fractures and deformed quartz rods along the shear zone. Inset equal area projection shows S_3 , fractures and stretching lineations L_3 measured along the shear zone; (b) map illustrates the sheared lithologies and individual markers used for measuring the displacement. Also shown are the positions of investigated sections across the shear zone; (c) γ vs. W_{sect} plots calculated for the sections in (b); SZC—shear zone centre. UTM 31T 521767 east, 4687430 north.

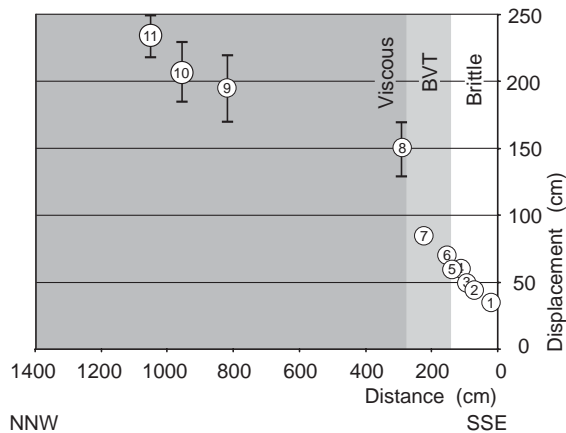


Fig. 6. Displacement vs. distance plot for the markers labelled in Fig. 5b. Note the continuous increase in displacement with increasing distance from the fault tip, especially across the transition from predominantly brittle fracturing to mylonitic shearing. The error bars represent broad and conservative estimates of the displacements that result from uncertainties due to the uneven outcrop morphology.

3.2. Shear zone nucleation and propagation

Fig. 5 shows the termination of a shear zone within metagreywackes and metapelites. The displacement of markers decreases continuously from the middle of the shear zone at the left to the tip at the right (Fig. 6). Based on the evaluation of displacements along single faults (e.g. Cowie and Scholz, 1992; Cowie and Shipton, 1998) as well as on microstructural observations (Fousseis and Handy, 2006), we interpret this relationship to show that the tip of the shear zone developed most recently, whereas the middle of the shear zone was active longer. Therefore, a succession of deformation increments can be studied from tip to middle along the length of the shear zone.

The actual shear zone termination consists of parallel shear fractures, typically between 50 and 150 cm long, which accommodate a fraction of the *total displacement* and cross-cut slightly refolded D_2 axial planes (arrow 1 in Fig. 5a). The fractures overlap and separate intervening volumes of less-deformed rock. $S_{1/2}$ sometimes appears to have rotated synthetically in these intervening domains. Microstructural investigations reveal that fractures contain narrow seams of fault rock consisting of aligned biotite, quartz and feldspar (Fousseis and Handy, 2006). Towards the left in Fig. 5, $S_{1/2}$ is increasingly dragged and becomes almost parallel to the D_3 shearing plane in its most strongly deflected, central part (arrow 2 in Fig. 5a). In this part of the shear zone, fractures are more closely spaced and segment the D_2 fabric. The total displacement in this domain is distributed among slip on closely-spaced shear fractures, on the deflected $S_{1/2}$, as well as on rotated $S_{1/2}$ between the fractures.

The relatively oldest, central part of the shear zone consists of smooth marginal drags and a mylonitic centre approximately 15 cm wide where most of the displacement is accommodated and no fractures occur. D_2 fabrics in ductile drags are gradually mylonitically overprinted towards the shear zone centre (Carreras and García-Celma, 1982; García-Celma, 1983). Significant grain-size reduction is observed. Layers of folded

$S_{0/1}$ rotate into parallelism with the D_3 shearing plane and are significantly thinned (arrow 3 in Fig. 5b). Nevertheless, individual markers (quartz rods and lithological beds) can be traced across the shear zone (Fig. 5b).

We quantified the strain evolution in 10 sections across the shear zone by measuring $S_{1/2}$ orientations and applying Ramsay and Graham's (1970) method of calculating the shear strain (γ) distribution (Appendix B). Slip on $S_{1/2}$ itself could not be quantified and thus was not considered in these calculations. Therefore, the calculated γ -values may be slight underestimates of the actual shear strain.

Curved drags indicate that γ is not distributed homogeneously across the shear zone (Ramsay and Graham, 1970). The *maximum shear strain* in the shear zone centre (γ_{\max}) was estimated using a procedure described in Appendix B. The *average shear strain* (γ_{mean}) was calculated by dividing the total displacement across a particular section by the local *shear zone width*, W_{sect} , at that section (data listed in Table 1).

Both γ_{mean} and γ_{\max} increase along the shear zone from SE to NW, from the shear zone termination to the mature segments. Due to the almost constant width of the shear zone, γ_{mean} increases almost linearly with displacement, from 0.2 at section 1 to 2.0 at section 10 in Fig. 5c. γ_{\max} increases non-linearly from 1.28 at section 1 to >37 at section 10, especially towards the left of section 4 (see Fig. 5b and c) where all displacement is accommodated within the centre of the mylonitic shear zone. We interpret this to indicate that strain softening occurred in the shear zone centre relative to the propagating tip.

Lateral terminations of metre- to decametre-long shear zones could not be mapped in the investigation area. However, we propose that these terminations look similar to the described leading and trailing terminations, since the mechanisms by which the rock deforms are the same. The varied orientation of $S_{1/2}$ with respect to the lateral shear zone terminations is a factor that may influence the geometry of the resulting tip process zone. However, the ductile beads that have been described from mode III terminations of thrust faults (Elliott, 1976) resemble the ones shown in this paper (Figs. 3–5).

3.3. Shear zone interconnection and strain homogenisation

Shear zones that exceed several metres in length are interconnected with neighbouring shear zones to form three-dimensional networks. These *shear zone networks* comprise interconnected, NW–SE-trending *host shear zones* and E–W-trending *step-over shear zones*, as observed in the southern Cala Serena (Fig. 7a). The most prominent host shear zone trends NW–SE through the centre of the mapped area (arrow 1 in Fig. 7a). It is connected to a sinistral step-over shear zone trending E–W (arrow 2 in Fig. 7a). Between the two, NW–SE-trending, decimetre- to metre-wide mylonitic host shear zones splay at a roughly regular 10–20 m distance from the sinistral shear zone (Fig. 7a). Most of these subordinate host shear zones have brittle terminations in the SE, which indicates that these narrower host shear zones nucleated along the sinistral master fault and propagated towards the SE. The host shear zones are

Table 1
Structural data from Sections 1–10 across the shear zone in Fig. 5b. The dataset documents a gradual increase in displacement from SE to NW, as well as increasing divergence between γ_{\max} and γ_{mean} . The shear zone width W_{sect} is approximately constant. Displacements were interpolated from Fig. 6. See Appendix A for terminology.

Section (NW < > SE)	10	9	8	7	6	5	4	3	2	1
Distance from SZ-tip (cm)	1570	1325	1220	1030	880	500	350	120	70	10
D_{sect} (cm)	324	279	261	225	200	131	104	60	45	30
W_{sect} (cm)	160	140	198	95	170	70	140	120	160	185
HW drag (from-to, cm)	–106 to –3	–55 to –5	–105 to –2	–32 to –9	–118 to –2	–50 to –8	–50 to –10	–55 to –65	–72 to 88	
HW damage zone displacement (cm)	52	21	39	13	39	17	31	56	102	40
FW drag (from-to, cm)	2 to 54	5 to 85	3 to 93	3 to 63	9 to 52	4 to 20	10 to 90	–	–	–
FW damage zone displacement (cm)	88	56	19	18	4	10	22	–	–	–
SZ Centre (from-to, cm)	–3 to 2	–5 to 5	–2 to 3	–9 to 3	–2 to 9	–8 to 4	–10 to 10	–	–	–
γ_{\max}	37	20	41	16	14	8.7	2.5	1.37	2.23	1.28
γ_{mean}	2.0	2.0	1.3	2.4	1.2	1.9	0.7	0.5	0.3	0.2

interconnected by several step-over shear zones. The lateral distance between the host shear zones is about half the along-strike distance between the step-overs. This initial network of host and step-over shear zones defines rhomb-shaped *lozenges* of less deformed rock with lengths between 15 and 30 m and widths of 5–10 m (Fig. 7a). $S_{1/2}$ in these lozenges is reoriented with respect to the undeformed domains outside the network (Fig. 7b). The orientations of all mylonitic shear zones and shear fractures are plotted in Fig. 7c.

Fig. 8 shows the poles to the D_3 shear zones and associated L_3 stretching lineations with respect to the overall shearing plane, C_3 . C_3 is depicted in a horizontal E–W orientation for reference (horizontal equator in Fig. 8). The asymmetry of the S_3 foliation poles with respect to C_3 is partly caused by step-over shear zones that emerge from host shear zones and connect them at an acute angle to the overall shear plane (Fig. 7). The overall pattern of S_3 and L_3 in Fig. 8 is diagnostic of a strong component of simple shearing during D_3 (Gapais et al., 1987; see below).

Most step-overs are parallel to $S_{1/2}$ (Fig. 9; small black arrows in Fig. 7) or cut $S_{1/2}$ at acute angles. Step-overs can be found in different evolutionary stages, from precursory brittle fractures without visible slip and without macroscopically visible fault rock (arrows in Fig. 7a), to narrow shear zones containing a black and very homogeneous, ultra-mylonitic fault rock (Fig. 9), to wider ductile shear zones with fine-grained, homogeneous mylonitic fabrics (Fig. 10). Similar to the host shear zones, we interpret this sequence of stages to represent a continuous evolution with increasing displacement. Unambiguous shear-sense indicators are rare in step-over shear zones, irrespective of scale. If shear sense indicators are found, then they are in roughly equal numbers of opposing indicators (Fig. 7a). We interpret this to indicate a complex deformation history (see Discussion section).

Some shear zones are wider and the lozenges between them are smaller (Figs. 12 and 13). We interpret wider shear zones to have accommodated more displacement than narrower ones. Shear-zone widening involves slip on and propagation of fractures cross-cutting the dragged foliation in the rock next to mylonitic shear zones in a process termed *drag truncation* (Fig. 11a and b). Fractures truncating drags can be found in the footwall as well as in the hanging wall of mylonitic shear zones (Fig. 5, arrows 4–6 and Fig. 11b, arrow 4). In some cases, these fractures link at their rear (NNW-most extent) with other fractures emerging from the mylonitic shear zone centre (arrow 1 in Fig. 11a), whereas in other cases they propagate towards the shear zone centres themselves (arrow 5 in Fig. 11b). The rock between the fracture and the shear zone centre is decoupled from the host rock (arrow 2 and shaded area in Fig. 11a, stars in Fig. 7). Fabrics within the isolated domains are usually reoriented with respect to the foliation outside. This reorientation involves a component of flexural slip parallel to $S_{1/2}$ (Carreras and García-Celma, 1982; García-Celma, 1983). Fractures that segment the drag are interpreted to have existed either prior to the onset of mylonitic shearing (e.g. arrow 3 in Fig. 3) or to have formed during dragging and mylonitic shearing. An example of drag truncation in Fig. 11 shows a

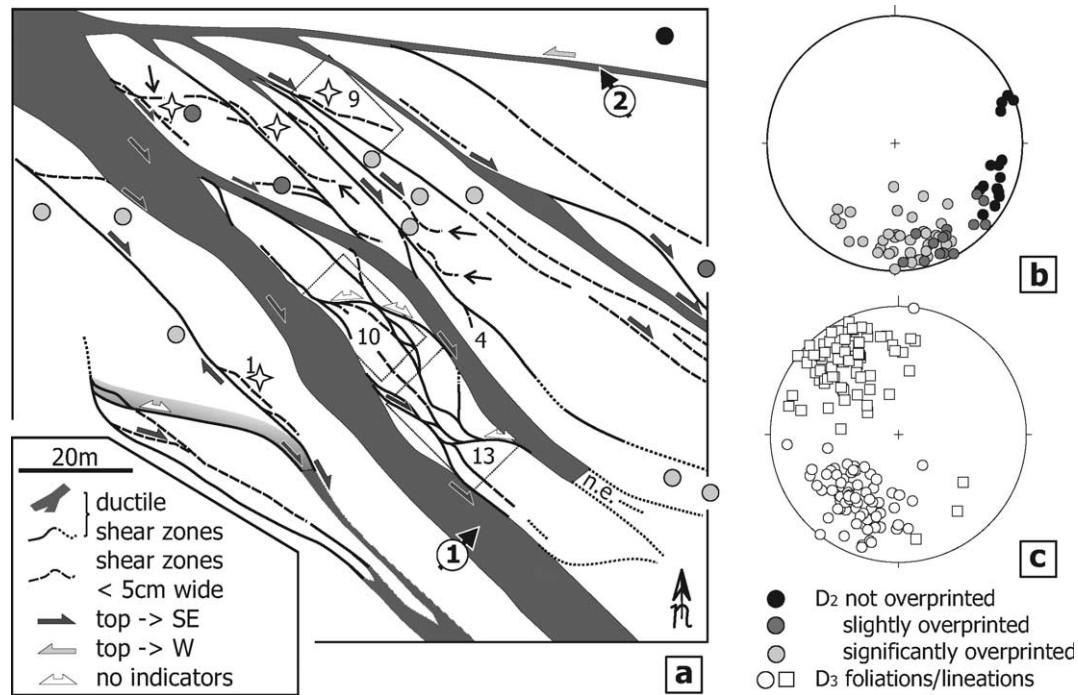


Fig. 7. Shear zone network in the SE part of the Cala Serena valley, where different stages of shear zone networking can be observed: (a) map of SZN. White inset boxes correspond to Figs. 9, 10 and 13. White circle labelled '4' marks the position of Fig. 4. Grey shaded and black circles correspond to sites where the orientation of $S_{1/2}$ was measured. Note that the intensity of shading corresponds to the qualitatively estimated intensity of D_3 overprint (black—*not overprinted*, light grey—*significantly overprinted*). White stars indicate outcrops where drag truncation can be observed. n.e.—*not exposed*; (b) equal area projection shows orientation of $S_{1/2}$ outside the SZN and in lozenges. See bottom right corner for colour codes. Dataset = 69 measurements; (c) equal area projection illustrating poles to D_3 shear zones (circles) and associated stretching lineations (squares). Dataset = 75 measurements. Database for slip line analysis in Fig. 8.

successive reorientation of the wall-rock foliation from the fault's propagating tip (right) towards its rear (left, Fig. 11a, inset equal area plot). The decoupled fabric experiences pronounced (D_3) mylonitic overprint during rotation. Reorientation and mylonitic overprint increase in intensity from left (NNW) to right (SSE) (see equal area plot in Fig. 11a). The rock at the left (rear) end of the truncated drag is macroscopically indistinguishable from the mylonite in the shear zone centre below. The subsidiary fault drag, which evolves along the NW end of the fracture, and its termination as a mode 1 fracture at the SE end indicate that the fracture propagated towards the right (SE).

Truncated drags are between 0.1 and 1 m wide and 0.2–8 m long (Figs. 7a and 11). There seems to be a relation between the scale of the truncated drags and the width of the involved shear zones, which could not be quantified yet. En-échelon arrays of truncated drags were observed in the Cala Serena (star 1 in Fig. 7a). Drag truncation occurs along step-over shear zones as well as along host shear zones and thus compartmentalizes lozenge interiors. Once the tips of fractures truncating the drags connect with other shear zones, the resulting compartments form smaller-scale lozenges. Fig. 10 shows a step-over that separates two lozenges. Towards its right and below its junction with the upper host shear zone, a number of smaller lozenges are isolated to form compartments (arrow 1 in Fig. 10), whereas compartmentalisation is not yet complete in other cases (arrows 2 and 3 in Fig. 10).

The degree of mylonitic overprint of the lozenge increases with decreasing angles between the bounding step-overs and the host shear zones (compare Figs. 10 and 12). Juvenile step-over shear zones in our investigation area, mostly brittle fractures and thin ultramylonites, are usually subparallel to undeformed D_2 -fabrics as long as the displacement is relatively small (see equal area plot in Fig. 9). Step-overs in highly overprinted rock are usually decimetre-wide mylonitic shear zones making a significantly smaller angle with C_3 (Fig. 12).

Compartmentalisation of lozenges and subsequent incorporation of lozenge rock into the mylonitic D_3 shear zones act in concert with the rotation of step-over shear zones to homogenise strain on the scale of the fracture network observed at the onset of interconnection. Fig. 13 shows an

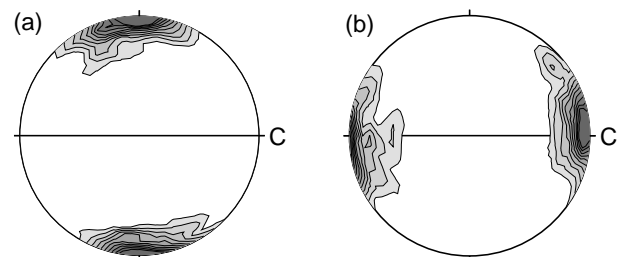


Fig. 8. Slip line analysis (method of Gapais and Cobbold (1987) and Gapais et al. (1987)) of the southern Cala Serena SZN: (a) poles to D_3 shear zones; (b) L_3 stretching lineations. 'C' indicates inferred macroscopic shearing plane oriented E–W for reference. Dataset 75, contours at 1, 2, 3, 4, 5, 6, 7, 8, 9 and 10% of a uniform distribution. See text for explanations.

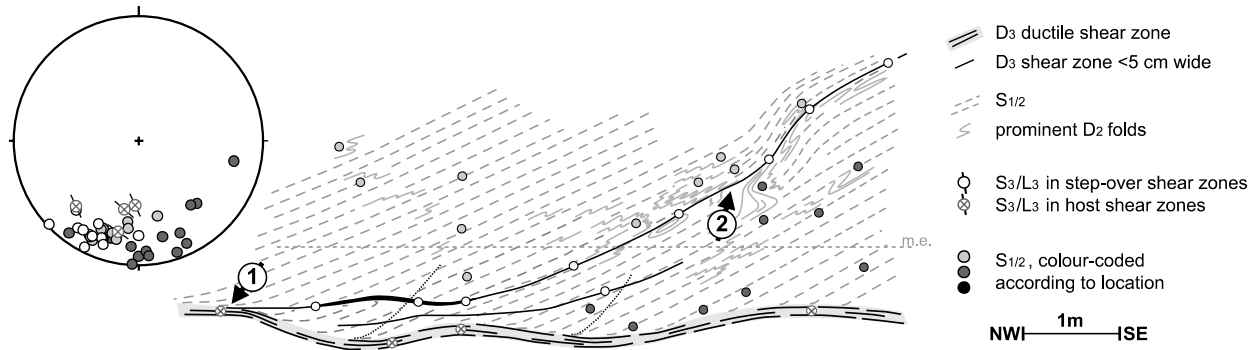


Fig. 9. Sketch map showing a step-over shear zone containing thin black ultramylonite that branches from a host shear zone at the left margin of the picture (arrow 1). The step-over shear zone follows $S_{1/2}$ (arrow 2). The equal area plot illustrates that the orientation of $S_{1/2}$ varies in the footwalls and hanging walls of the step-over shear zone. The step-over itself is parallel to the hanging wall fabrics. Note the shading of different fabric domains. S_3/L_3 orientations for mylonitic shear zones are plotted with the method of Hoepfner (1955). m.e. indicates a morphological edge of the outcrop. Legend applies to Figs. 10 and 13. UTM 31T 521933 east, 4686984 north.

advanced stage of this homogenisation process. The volume proportion of D_3 mylonite (shaded, black foliation trajectories) roughly equals that of less-deformed host rock (white areas, grey, dashed foliation trajectories). Drags in the lozenges are truncated by fractures (arrow 1 in Fig. 13).

The northernmost part of the Cala Serena (fig. 8 in Carreras, 2001) shows a mature stage of network evolution, where the volume proportion of D_3 mylonites is relatively large and deformation is almost homogeneous on a scale of several tens of metres. A single D_3 shear zone—almost 50 m wide—contains only small-scale lozenges up to 3 m in length.

4. Discussion and interpretation

4.1. Evidence for a strain dependent BVT

Several arguments indicate that fracturing occurred coevally with mylonitisation during retrograde deformation at temperatures between 400 and 500 °C (Fousseis and Handy, 2006):

- (1) Most of the observed fractures, irrespective of their occurrence individually or in damage zones, are parallel to mylonitic fabrics of the ductile shear zones (equal area plot 1

in Fig. 5a). Ductile beads as well as drags near brittle fractures indicate the same movement sense as obtained from independent kinematic indicators within the ductile shear zones (Figs. 3 and 4). None of the fractures in these orientations were seen to cross-cut or overprint D_3 mylonites, neither on the outcrop nor on the microscopic scales (Fousseis and Handy, 2006). Brittle overprinting of D_3 fabrics is restricted to D_4 faults that possibly formed during E–W Tertiary extension of the area (e.g. Mauffret et al., 2001). Hydrothermal alterations and the kinematics of these D_4 faults clearly allow one to distinguish them from D_3 fractures.

- (2) The displacement–distance relationship in Fig. 6 clearly shows a constant increase in displacement going from the fractures to the mylonite, as shown in Fig. 5. If fractures had nucleated at the tips of mylonitic shear zones after mylonitisation, they would be expected to have developed independent, symmetrical displacement–distance profiles (cf. Cowie and Shipton, 1998 and references therein).
- (3) The process of drag truncation involves both brittle fractures and mylonitic shear zones. Even though we do not know if the drags were fractured during mylonitic shearing or the fractures are reactivated remnants of fractures formed early

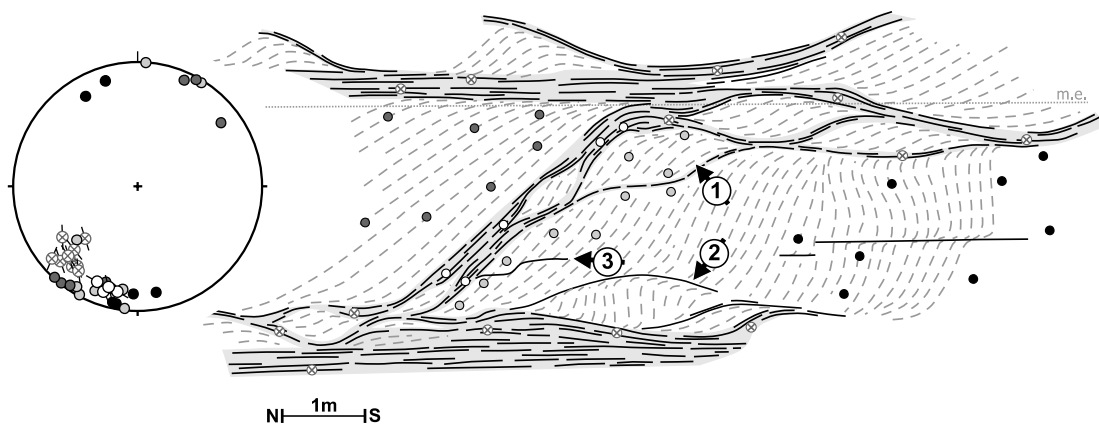


Fig. 10. A step-over shear zone linking two host shear zones. Small lozenges form along the step-over shear zone. The equal area plot shows the orientations of S_3/L_3 (projection method of Hoepfner (1955)) as well as $S_{1/2}$ orientations adjacent to the shear zones. Note the shading of different fabric domains. Legend as in Fig. 9. UTM 31T 521937 east, 4686951 north.

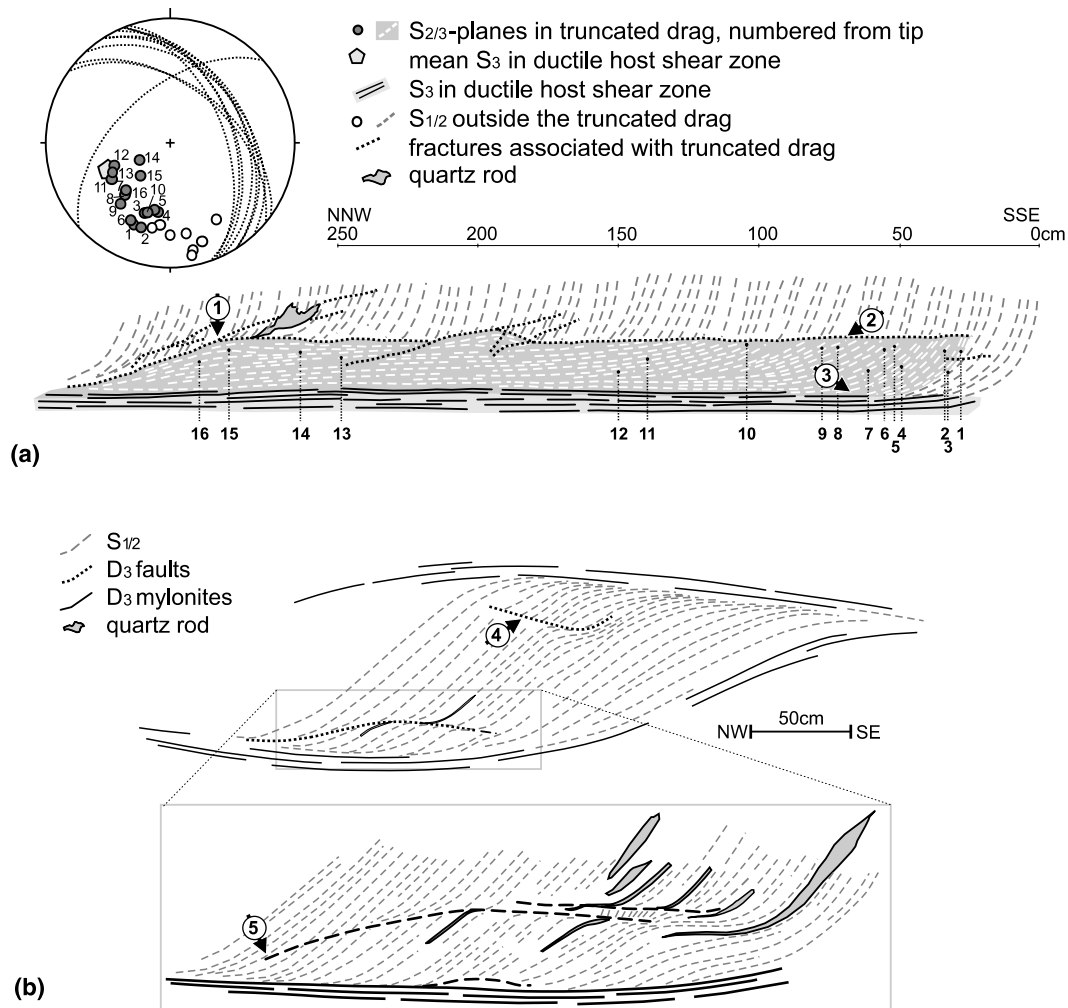


Fig. 11. Shear zone widening: (a) A shear zone boundary in Cala Prona reveals the 'drag truncation' process. The lower hemisphere, equal area plot shows the foliation orientation within the isolated domain and its rotation into parallelism with the host shear zone at the bottom; UTM 31T 521755 east, 4687572 north. (b) Sketch of a lozenge in the Cala Serena illustrating drag truncation on a smaller scale within a lozenge in a mature mylonitic shear zone. Note the drag truncation at the top of the lozenge (arrow 4). UTM 31T 521585 east, 4687106 north.

during D₃, synkinematic fractures segment parts of ductile drags. The reoriented fabrics within these segmented, isolated domains experienced a greater degree of mylonitic overprint and thus are enveloped within the broadening shear zones (Fig. 11a). Therefore, fracturing is an integral process in the widening of mylonitic shear zones.

- (4) Microstructural investigations indicate upper-greenschist facies conditions for the formation of centimetre-scaled fractures in tip damage zones of mylonitic shear zones, which are in structural continuity with quartz-rich parts of the rock undergoing increased dynamic recrystallisation by bulging and subgrain rotation (Fousseis and Handy, 2006).

4.2. A model for the formation, propagation and networking of shear zones at the BVT

Having established that fracturing and viscous mylonitic creep were coeval, we advance the following propagation

model for shear zones at the BVT (Fig. 14a): pre-D₃ fabric domains are expected to have shown heterogeneous mechanical behaviour during loading. Initial flaws nucleated at pre-existing heterogeneities. These flaws are interpreted as predominantly mode 2 fractures, because they show little to no dilation and are parallel to the later shear zones. Creep in the ductile beads in front of the fault tips is interpreted to have dissipated some of the strain energy stored during loading and lead to localised softening there. However, the rate of stress relaxation in the ductile beads was less than the overall rate of loading, so that the brittle strength of the rock at the fault tip was exceeded and the fracture propagated into its viscously deforming process zone. Such episodic frictional instability leading to faulting during creep has been discussed recently by Handy and Brun (2004).

Brittle fractures are not longer than about 7–8 m in any of the investigated sites and no isolated, mylonitic shear zones were found that are shorter than this length. Therefore, it stands to reason that once a growing fault system acquired a

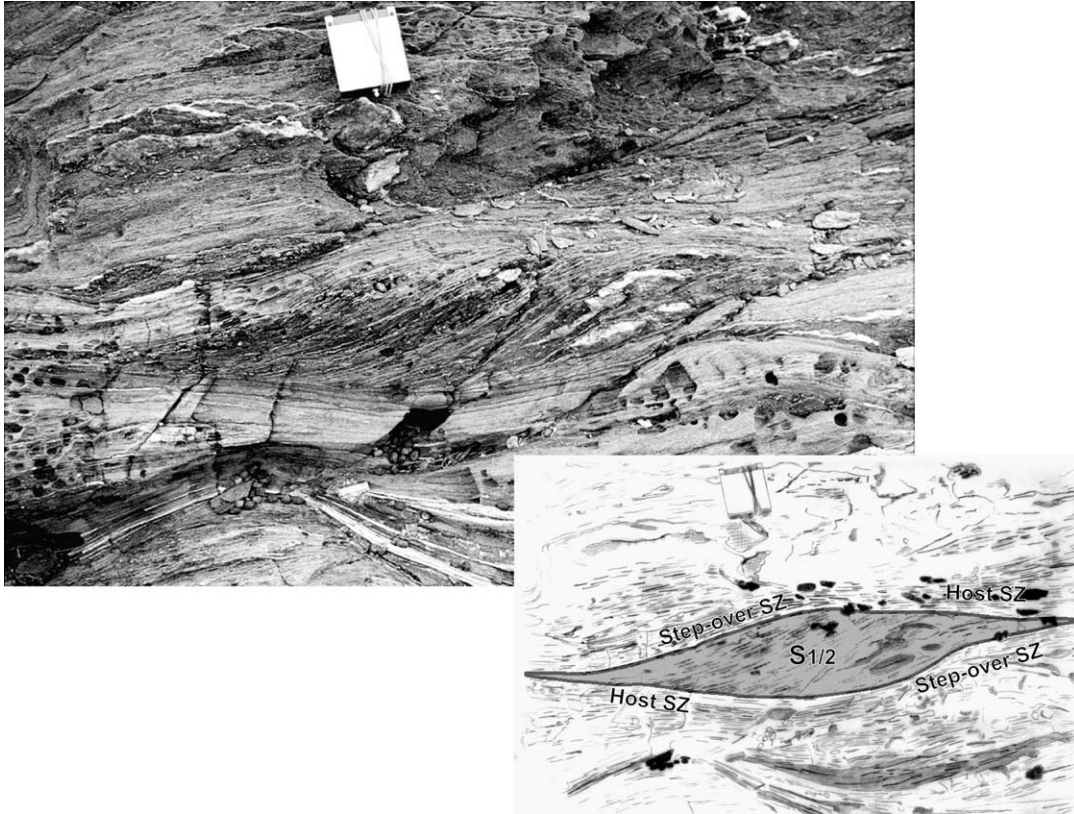


Fig. 12. Mature lozenge in a highly deformed part of the Cala Serena SZN. Pre-D₃ mineral assemblages are preserved in the lozenge interior (notice coarse grain size), whereas the material in the surrounding host and step-over shear zones experienced a significant D₃ mylonitic overprint. Compass for scale, side length ~8 cm. Location in inset '12' of Fig. 1. UTM 31T 521687 east, 4686903 north.

critical length and displacement, mylonitic shearing replaced episodic fracturing as the dominant deformation mechanism. The transition was controlled by the combined effects of brittle segmentation of the ductile bead at ambient temperatures of >400 °C, dynamic recrystallisation of quartz and syntectonic recrystallisation of biotite, which together softened the host rock in the tip process zone (Fig. 5; Fousseis

and Handy, 2006). There is no evidence for a major influx of externally derived hydrous fluids. Shear zone evolution documented in Fig. 5 indicates that the critical total displacement necessary to soften the host rock sufficiently for a transition from predominantly brittle to viscous deformation was around 120 cm along a 140-cm-wide shear zone.

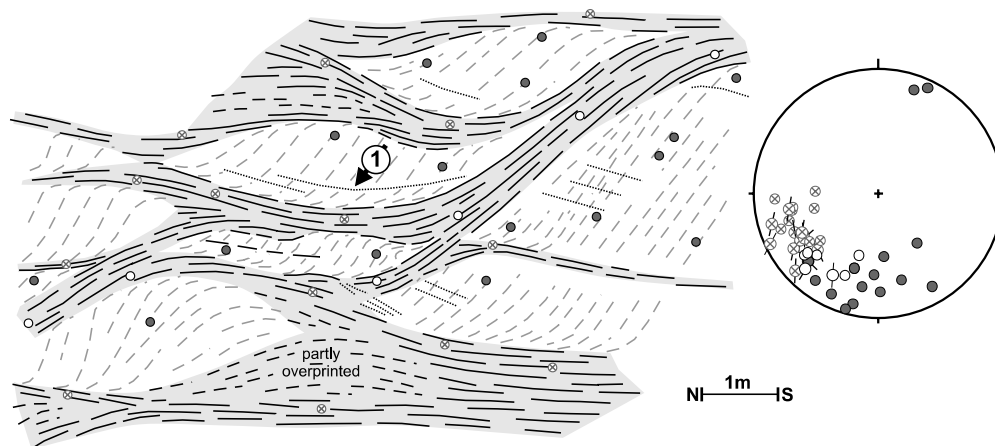


Fig. 13. Mature pattern of interconnected shear zones. The remaining D₂ domains are progressively incorporated into the D₃ shear zones. Note fractures in dragged margins of the lozenges. The lower hemisphere, equal area plot shows the orientations of S₃/L₃ (projection method of Hoepfner (1955)) as well as S₂ orientations adjacent to the shear zones. Note the shading of different fabric domains. Legend as in Fig. 9. UTM 31T 521948 east, 4686935 north.

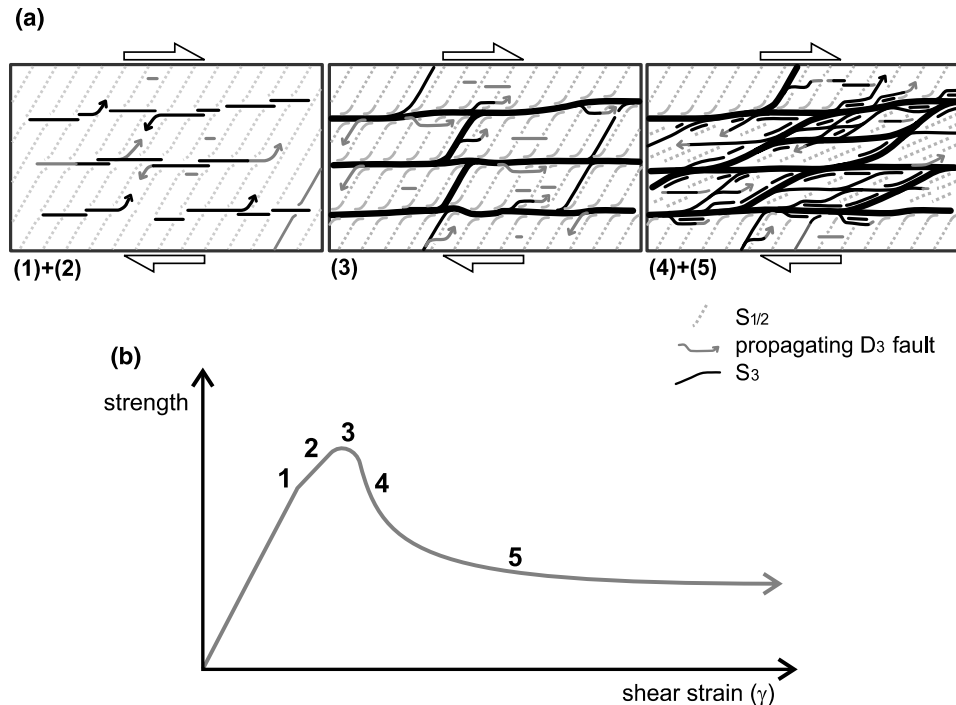


Fig. 14. Model for the structural and mechanical evolution of shear zone networks on a 10^2 – 10^3 m scale: (a) fracture propagation and coalescence of shear zones corresponding to the mechanical evolution in (b); (b) inferred evolution of rock strength with progressive shear strain. See text for explanations.

The sharp cut-offs of normal drags along many drags indicate that the drags formed when fractures propagated through ductile beads (de Margerie and Heim, 1888; Elliott, 1976). The detailed shape, curvature and dimension of beads and consequently of drags were influenced by the deformed lithology as well as by interaction and interconnection with other fractures (Fig. 4). The formation of mylonitic shear zone centres during a strain-dependent BVT transformed sharp cut-offs into smooth cut-offs. This modified the drag shape.

We interpret the step-overs to have formed due to strain compatibility requirements that arose from accumulating displacement along the host shear zone, in analogy with the model proposed by Mitra (1979). Rotating step-over shear zones forced the intervening lozenges to deform internally. This effect was strongest at the intersections between step-over and host shear zones, which was where most compartments were observed (Figs. 10 and 13).

The question why softening shear zones widen by drag truncation is crucial. Fractures that already existed within the damage zone of a mylonitic shear zone would have eased rotation and thus mylonitic overprint of $S_{1/2}$ in these domains. Fractures that truncated existing drag and propagated during shearing (which is supported by field evidence; Fig. 11a) indicate a competition between the rate of strain energy dissipation in the shear zone centre and the loading rate of the system, similar to the model proposed above for the fault propagation in ductile beads.

The overall driving mechanism for shear zone widening may be a combination of strain energy minimisation and maintenance of strain compatibility. If the shear zones can be compared with slip systems in crystals (as proposed by Mitra

(1979)), then applying Von Mises' criterion to our (plane strain) case would support the idea that the two shear zone types (host and step-over shear zones) are insufficient in number to accommodate the bulk shearing compatibly. A third independent shear zone orientation does not form, possibly because shear zone widening by rotation of $S_{1/2}$ into the shearing plane allows bulk deformation to become heterogeneous on a larger length scale, thereby expending less bulk strain energy per unit volume and time and maximizing the rate of strain energy dissipation per unit volume of deforming rock. As a consequence, the length scale of heterogeneous strain increases with displacement.

4.3. Bulk kinematics and scales of strain localisation

Carreras (2001) invoked analogue models of folded anisotropies (Cobbold et al., 1971; Cosgrove, 1976, 1989; Williams and Price, 1990) to propose buckling instabilities as the prime nucleation mechanism for the shear zones in the 'Northern Shear Belt' (cf. Fig. 18 in Carreras, 2001). Carreras argued that the instantaneous shortening direction for D_3 (ISA_3^-) was oriented approximately N–S. Depending on the orientation of $S_{1/2}$ with respect to this ISA_3^- , different shear zone geometries resulted from the rotation and shearing of the limbs of folds that formed due to buckling of $S_{1/2}$. In areas like ours where the initial angle between the inferred ISA_3^- and the ENE–WSW-trending $S_{1/2}$ was high ($\sim 80^\circ$), Carreras (2001) proposed that a single set of dextral shear zones initiated close to the direction of maximum instantaneous stretch and rotated into parallelism with the bulk shearing plane, which trends approximately NW–SE. In areas where the angle between $S_{1/2}$

and the ISA_3^- was small, a conjugate set of shear zones evolved, with synthetic shear zones nucleating close to the bulk shearing plane and antithetic shear zones close to the plane of maximum instantaneous shear strain, nearly normal to the shearing plane (fig. 18 in Carreras, 2001).

The buckling model of shear zone formation (Carreras, 2001) explains the orientation of the host shear zones in the investigated area, but it is incompatible with the E–W-trending step-over shear zones and does not explain the close association of fractures and mylonitic shear zones. Furthermore, we note that the E–W-trending step-overs and host shear zones did not nucleate coevally. Rather, the step-overs are usually younger, as they branch from the better-developed, host shear zones that accommodated more deformation.

The step-over shear zones nucleated at angles of about 60–80° to the bulk shearing plane, C_3 , suggesting that $S_{1/2}$ at high initial angles to C_3 guided the propagation of juvenile step-overs, as described above. Shear zones with this orientation are expected to have accommodated sinistral shear in the bulk dextral regime. With increasing bulk deformation, the step-overs rotated across ISA_3^+ towards C_3 . Upon crossing this axis, they accommodated pure shear before their shear sense changed to dextral, as observed in experiments on networked shear zones formed in noncoaxial shear (Herwegh and Handy, 1996, 1998) and proposed by Carreras (2001, see his fig. 18). This may explain the ambiguous shear sense indicators in most of the step-over shear zones.

The orientational distribution pattern of networked shear zones in Fig. 8 reflects both the kinematic vorticity and the shape of the finite strain ellipsoid during D_3 (Gapais et al., 1987). As pointed out above, the slight asymmetry of the maxima for the poles to S_3 reflects the orientations of the host- and step-over shear zones with respect to the shearing plane. The broad single maximum of the poles to S_3 (Fig. 8a) indicates that the lozenges are oblate; their asymmetry indicates non-coaxial shearing. The single maximum in the L_3 equal area plot points towards a stretching direction typical of near plane-strain deformation (Fig. 8b). Considered together, the orientational distribution pattern is diagnostic of strongly non-coaxial nearly plane-strain dextral shearing during D_3 (Gapais et al., 1987; Handy et al., in press). We note that this justifies our generalizations about shearing made from the study of strain in two dimensions.

4.4. Implications for crustal strength at the BVT

The strength of the crust affected by shear zone networking at the BVT is expected to have decreased significantly during strain localisation (Fig. 14b). The nucleation of shear fractures in the host rock is inferred to have coincided with yielding (pt. 1 in Fig. 14b). Continued loading promoted fracture lengthening, incipient interconnection and the accumulation of displacement. Mylonite formed after the fractures reach a critical length and displacement (respectively, 7–8 m and 80–120 cm in our examples). Grain-size reduction involving dynamic recrystallisation and the nucleation and growth of weaker phases (mica) weakened the

shear zone, focussing deformation along its central, high-displacement segment and reducing the rate at which strain energy accrued in the deforming system (pt. 2 in Fig. 14b). Because viscous creep is rate-strengthening (e.g. Scholz, 1988), mylonitisation prevented run-away weakening and dampened stress pulses associated with fracturing at the shear zone tips.

The peak strength of the deforming system is predicted to have coincided with the maximum number of isolated fractures and ductile shear zones per volume of deforming rock, i.e. the state of the system just prior to full networking (pt. 3 in Fig. 14b). This is when the aspect ratio of isolated shear zones and the maximum number of propagating tips reached a maximum. We note that the onset of localisation prior to the attainment of peak strength predicted for the fossil BVT at the Cap de Creus is consistent with the behaviour of some dilatant materials, including viscoplastic materials whose deformation involves limited dilatancy (Hobbs et al., 1990).

The coalescence of individual shear zones lead to the formation of a three-dimensional network, as described in the previous sections. Networking is expected to have induced a rapid drop in strength of the deforming system (curve from pts. 3 to 4 in Fig. 14b) once the networked mylonitic shear zones formed an interconnected weak layer subparallel to the bulk shearing plane. A strength drop due to networking of weak phases has been proposed based on theoretical considerations and experiments on two-phase aggregates (e.g. Handy, 1990, 1994 and references therein). A possible reason for the networking could be the necessity to maintain strain compatibility within the deforming system, i.e. the entire rock including the shear zones and the existing $S_{1/2}$ (Mitra, 1979). Our observations indicate that juvenile shear zone networks are about 50–100 m wide and maintained this overall width with continued deformation. Within this limit, the networked shear zones widened, promoting continued overall weakening (curve from pts. 4 to 5 in Fig. 14b) as the volume proportion of weak, mylonitic rocks increased in the deforming system (Handy, 1994). A factor controlling shear zone widening may be the rotation of the step-over shear zones, which required overprinting of the lozenge interiors.

The rate of weakening is expected to have decreased until some stable volume proportion of sheared rock was reached, or when all un- or less-deformed host rock in the lozenges was incorporated in D_3 shear zones. At this stage, strain homogenised on the length scales of fracturing and networking, but became heterogeneous on all larger length scales. Therefore, rock strength must be considered to be strongly scale-dependent.

5. Conclusions

Brittle faults were precursors to mylonitic shear zones in the shear zone networks at the fossil BVT exposed at the Cap de Creus, NE Spain. Fracturing was accompanied by viscous mylonitic deformation of the host rock in ductile damage zones surrounding the fractures. Brittle segmentation and the

mylonitic overprint of host rock in these damage zones lead to a strain-dependent transition from brittle faulting to mylonitic shearing. This is inferred to have involved strain-softening. Once ductile shear zones formed, drag-truncation, involving brittle fracturing, allowed shear zones to continue widening on scales from decimetres to several metres while they experienced strain softening.

Interconnection of shear zones and fractures was influenced by the existing foliation orientated at high angles to the shearing plane. This foliation guided the propagating fracture tips. Initial shear zone networks are defined by lozenges, some 10–20 m long and 5–10 m wide. The lozenges between the networked shear zones were progressively compartmentalized by drag truncation and incorporated into the shearing volume of rock. Finally, strain became homogeneous at the initial length scale of networking.

The strength evolution of the crust at the BVT is governed by the transition from predominantly brittle fracturing to mylonitic shearing, the interconnection of individual shear zones to form networks and the homogenisation of deformation on the scale of those networks. Strain localisation in shear zone networks can be expected to weaken the crust on the scale of these networks by up to 20% (Handy, 1994).

Acknowledgements

We thank Jordi Carreras and Elena Druguet for their generous support in organizing field campaigns, aerial photographs and permits from the national park authorities.

They also kindly supplied several unpublished maps and data and provided fruitful discussions and comments on our work. Victoria Riera and the national park authorities are thanked for their uncomplicated support. Many thanks also to Ian Alsop and Jonathan Imber for their helpful and vigilant reviews, as well as to an anonymous reviewer for some critical points. We especially want to thank Bob Holdsworth for his mindful editing of the manuscript. Finally, we thank Roland Christmann and several students from the Freie Universität Berlin who contributed to this work with their help in the field and at home. Our work was supported by DFG grant Ha 2403/6 and by the Freie Universität Berlin in the form of a post-graduate studentship.

Appendix A. Terminology

The **brittle-to-viscous** transition is the change from fracturing on one or more discrete surfaces to thermally activated creep within zones of viscous, solid-state flow (Schmid and Handy, 1991; Handy et al., in press). Following Ramsay and Huber (1983), we distinguish between **brittle shear zones** (synonymous with **faults, fractures**) and **ductile shear zones**. *Shear zone* without a prefix is a general term describing any zone with sub-parallel walls in which deformation is localised. We use the term *ductile* exclusively in relation to solid-state viscous, mylonitic deformation, being fully aware that ductility itself is not a mechanistic concept (Rutter, 1986; Schmid and Handy, 1991). Wherever special

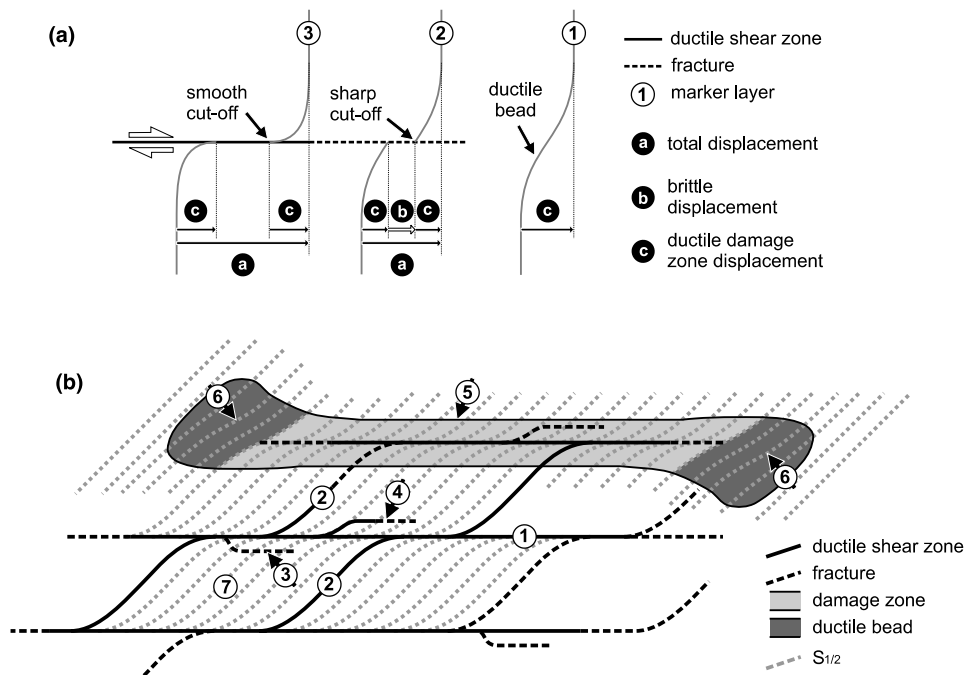


Fig. 15. Features of shear zones and shear zone networks: (a) a mylonitic shear zone with a brittle tip. Deflected marker layers illustrate the monoclinical fold forming the ductile bead beyond the tip of the brittle fault (marker 1); a sharp cut-off towards the fault plane (marker 2) and a smooth cut-off towards the mylonitic shear zone centre (marker 3). Note the difference between the brittle displacement, the ductile damage zone displacement and the total displacement; (b) a shear zone network with host shear zones (1), step-over shear zones (2), a footwall drag truncation (3), a hanging wall drag truncation (4), the ductile damage zone (5) and a ductile bead (6) around the host shear zone.

emphasize on deformation mechanisms is needed, we add appropriate prefixes.

Brittle shear zones show strain discontinuities across the shearing plane (marker 2 in Fig. 15a), whereas ductile shear zones show continuous variations of strain across their width and no geometrical discontinuities can be seen on the scale of the shear zone (marker 3 in Fig. 15a).

Finite strain across ductile shear zones increases continuously from zero strain and displacement at the margins of the shear zone to maximum strain and displacement in its centre. Brittle shear zones focus deformation on the shearing plane itself, but in most cases a volume of wall rock adjacent to the plane is deformed due to “the initiation, propagation, interaction and build-up of slip along faults” (Kim et al., 2004). In the fault mechanics literature, this volume is termed the ‘damage zone’. Where markers are oriented at high angles to the fault as in this study, most of this deformation in the wall rock near the fault is expressed macroscopically as monoclinally folded markers, here termed (**ductile**) **fault drags**. The rock volume where such fault drags occur is termed the **ductile damage zone** (Figs. 3 and 4 and see arrow 5 in Fig. 15b). The fault drag is **normal** when the deflection of markers is convex in the direction of shear along the fault or shear zone (marker 3 in Fig. 15a), and is **reverse** when the deflection in the direction of shear is concave (Hamblin, 1965). The intersection between a dragged linear or planar marker and the fault plane is called a **cut-off** (Ramsay and Huber, 1983). The nature of cut-offs is important in the context of strain gradients and the transition from faults to ductile shear zones and we therefore distinguish between **smooth cut-offs** where the tangent to the deflected marker at the cut-off encloses an angle β with the shearing plane of $<5^\circ$ (Fig. 15a) and **sharp cut-offs** where $\beta > 5^\circ$ (see markers in Figs. 4 and 15a). Deflections of planar or linear markers next to a structural element cross-cutting the rock (e.g. a fault) have been named ‘flanking structures’ (Passchier, 2001).

Monoclinical folds that form beyond the tips of brittle faults in the direction of tip propagation are termed **ductile beads**, following Elliott (1976). Elliott observed ductile beads in front of mode III fractures at the terminations of thrust faults. The ductile bead is part of the ductile damage zone (arrow 6 in Fig. 15b).

Displacement accommodated by ductile deformation in mylonitic shear zones is called **ductile displacement**. Displacement that is accommodated by ductile fault drags is called **ductile damage zone displacement** (‘c’ in Fig. 15a). Displacement accommodated by slip on brittle fault planes is termed **brittle displacement** (‘b’ in Fig. 15a). The sum of all displacements at a section across a shear zone—brittle and/or ductile—is the **total displacement**, D_{sect} (‘a’ in Fig. 15a). Distinguishing these different kinds of displacement is important when describing coeval discrete and distributed deformation.

The **width** of a shear zone, W_{sect} , is measured perpendicular to the shearing plane. Shear strain distribution in shear zones reaches a maximum, γ_{max} , within the shear zone and can be averaged across the entire shear zone by dividing the total

displacement by the width ($\gamma_{\text{mean}} = D_{\text{sect}}/W_{\text{sect}}$; see Appendix B).

Shear zone networks consist of interconnected host- and step-over shear zones. **Host shear zones** are parallel to the bulk shearing plane (‘1’ in Fig. 15b). **Step-over shear zones** connect host shear zones at an angle to the overall shearing plane (‘2’ in Fig. 15b). Host and step-over shear zones isolate **lozenges** of less deformed host rock in between (‘7’ in Fig. 15b). Shear zones are found to widen by **drag truncation**, a process involving lateral branching of fractures along ductile shear zones into fault drags, combined with rotation and overprinting of the fabric in the sheared domains between the fault and the shear zone centre. Drag truncation forms **truncated drag folds** or **truncated drags** (‘3’ and ‘4’ in Fig. 15b).

Appendix B. Quantifying γ_{max} in shear zone centres

We measured the orientation of the existing $S_{1/2}$ foliation along 10 sections approximately perpendicular to the shear zone. The angle between the deflected $S_{1/2}$ and the shear zone boundary (α') at a particular distance from the shear zone centre was used to calculate shear strain (γ)/shear zone width (W_{sect})-diagrams (Fig. 5c) after Ramsay and Graham (1970):

$$\cot \alpha' = \cot \alpha - \gamma \quad (1)$$

where α is the angle between $S_{1/2}$ and the shear zone boundary C_3 before being sheared. This technique was developed for passive markers only and using it for actively deforming markers—as shown for $S_{1/2}$ by Carreras and García-Celma (1982)—bears the risk of underestimating the finite shear strain. Nevertheless Eq. (1) gives a first-order estimate of γ .

Reliable γ values cannot be calculated near the shear zone centre, because the angles between the deflected (and reactivated) $S_{1/2}$ and C_3 are very small, such that even small measurement errors render very large perturbations of γ . To calculate the maximum shear strain (γ_{max}) in these central parts of the shear zone, we constructed γ/W_{sect} -diagrams from the margins towards the shear zone centre, as far as reliable measurements could be made (a and b in Fig. 16). We approximated functions $f(+x)$ and $f(-x)$ for the two scatterplots resulting from measuring the deflection of $S_{1/2}$ in the two fault drags. We then integrated these functions with respect to distance from the shear zone margins to the centre:

$$A_x = \int_{+x}^b f(+x) dx \quad (2)$$

and

$$B_y = \int_{-x}^a f(-x) dx \quad (3)$$

The area beneath the γ/W_{sect} -function equals the shear zone’s total displacement at that particular site (D_{sect} ; Ramsay

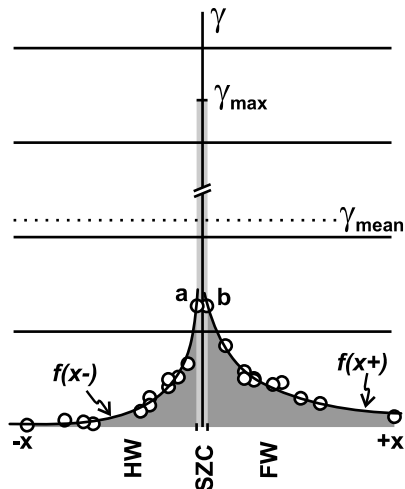


Fig. 16. Shear strain vs. width (γ/W_{sect}) diagram. FW—footwall, HW—hanging wall, SZC—shear zone centre. The shear strains were calculated using the equation of Ramsay and Graham (1970). The area of the grey rectangle in the shear zone centre equals the part of the total displacement that was not accommodated by shearing in the drags. The rectangle represents a conservative approximation of the shear strain distribution in the shear zone centre. See text for detailed explanation.

and Graham, 1970), which can be estimated from independent measurements. Therefore,

$$C = D_{\text{sect}} - (A_x + B_y) \quad (4)$$

where C is a rectangle whose base \overline{ab} is the width of the shear zone centre and whose length is a minimum estimate for γ_{max} (Fig. 16).

The mean shear strain (γ_{mean}) accommodated by the shear zone along a given transect was calculated with the relation

$$\gamma_{\text{mean}} = D_{\text{sect}}/W_{\text{sect}} \quad (5)$$

References

- Arbaret, L., Burg, J.P., 2003. Complex flow in lowest crustal, anastomosing mylonites: strain gradients in a Kohistan gabbro, northern Pakistan. *Journal of Geophysical Research—Solid Earth* 108 (B10), 2467–2484.
- Bell, T.H., 1981. Foliation development: the contribution, geometry and significance of progressive, bulk, inhomogeneous shortening. *Tectonophysics* 75, 273–296.
- Bons, P.D., Druguet, E., Hamann, I., Carreras, J., Passchier, C.W., 2004. Apparent boudinage in dykes. *Journal of Structural Geology* 26 (4), 625–636.
- Carreras, J., 2001. Zooming on Northern Cap de Creus shear zones. *Journal of Structural Geology* 23 (9), 1457–1486.
- Carreras, J., Casas, J.M., 1987. On folding and shear zone-development: a mesoscale structural study on the transition between two different tectonic styles. *Tectonophysics* 135 (1–3), 87–98.
- Carreras, J., García-Celma, A., 1982. Quartz c-axis fabric variation at the margins of a shear zone developed in schists from Cap de Creus (Spain). *Acta Geológica Hispánica* 17, 137–149.
- Carreras, J., Druguet, E., Griaer, A., 2005. Shear zone-related folds. *Journal of Structural Geology* 27 (7), 1229–1251.
- Choukroune, P., Gapais, D., 1983. Strain pattern in the Aar Granite (Central Alps)—orthogneiss developed by bulk inhomogeneous flattening. *Journal of Structural Geology* 5 (3–4), 411–418.
- Cobbold, P.R., Cosgrove, J.W., Summers, J.M., 1971. Development of internal structures in deformed anisotropic rocks. *Tectonophysics* 12 (1), 23–53.
- Cosgrove, J.W., 1976. The formation of crenulation cleavage. *Journal of the Geological Society* 132, 155–178.
- Cosgrove, J.W., 1989. Cleavage, folding and the finite strain ellipsoid. *Proceedings of the Geological Association* 100, 461–479.
- Cowie, P.A., Scholz, C.H., 1992. Physical explanation for the displacement-length relationship of faults using a post-yield fracture mechanics model. *Journal of Structural Geology* 14 (10), 1133–1148.
- Cowie, P.A., Shipton, Z.K., 1998. Fault tip displacement gradients and process zone dimensions. *Journal of Structural Geology* 20 (8), 983–997.
- de Margerie, E., Heim, A., 1888. *Les dislocations de l'écorce terrestre*. J. Wurster, Zürich.
- Dennis, A.J., Secor, D.T., 1987. A model for the development of crenulations in shear zones with applications from the Southern Appalachian Piedmont. *Journal of Structural Geology* 9 (7), 809–817.
- Druguet, E., 2001. Development of high thermal gradients by coeval transpression and magmatism during the Variscan orogeny: insights from the Cap de Creus (Eastern Pyrenees). *Tectonophysics* 332 (1–2), 275–293.
- Druguet, E., Hutton, D.H.W., 1998. Syntectonic anatectic and magmatism in a mid-crustal transpressional shear zone: an example from the Hercynian rocks of the eastern Pyrenees. *Journal of Structural Geology* 20 (7), 905–916.
- Druguet, E., Passchier, C.W., Carreras, J., Victor, P., den Brok, S., 1997. Analysis of a complex high-strain zone at Cap de Creus, Spain. *Tectonophysics* 280 (1–2), 31–45.
- Elliott, D., 1976. Energy-balance and deformation mechanisms of thrust sheets. *Philosophical Transactions of the Royal Society of London Series A—Mathematical Physical and Engineering Sciences* 283 (1312), 289–312.
- Fousseis, F., Handy, M.R., 2006. Grain-scale processes and inferred stress drops during the formation of shear zone networks at the brittle-to-viscous transition (BVT). *Geophysical Research Abstracts* 8, April 2–7 2006, EUG General Assembly, Vienna, Austria.
- Gapais, D., Cobbold, P.R., 1987. Slip system domains 2. Kinematic aspects of fabric development in polycrystalline aggregates. *Tectonophysics* 138 (2–4), 289–309.
- Gapais, D., Bale, P., Choukroune, P., Cobbold, P.R., Mahjoub, Y., Marquer, D., 1987. Bulk kinematics from shear zone patterns—some field examples. *Journal of Structural Geology* 9 (5–6), 635–646.
- García-Celma, A., 1983. C-axis and shape fabrics in quartz mylonites of Cap de Creus (Spain): their properties and development. Unpublished PhD thesis, University of Utrecht.
- Gilbert, L.E., Scholz, C.H., Beavan, J., 1994. Strain localization along the San Andreas fault: consequences for loading mechanisms. *Journal of Geophysical Research* 99 (B12), 23975–23984.
- Hamblin, W.K., 1965. Origin of “reverse drag” on the down-thrown side of normal faults. *Geological Society of America Bulletin* 76, 1145–1164.
- Handy, M.R., 1990. The solid-state flow of polymineralic rocks. *Journal of Geophysical Research—Solid Earth and Planets* 95 (B6), 8647–8661.
- Handy, M.R., 1994. Flow laws for rocks containing 2 nonlinear viscous phases—a phenomenological approach. *Journal of Structural Geology* 16 (3), 287–301.
- Handy, M.R., Brun, J.P., 2004. Seismicity, structure and strength of the continental lithosphere. *Earth and Planetary Science Letters* 223 (3–4), 427–441.
- Handy, M.R., Hirth, G., Bürgmann, R., in press. Fault structure and rheology from the frictional–viscous transition downward. In: Handy, M.R., Hirth, G., Hovius, N. (Eds.), *Dahlem Workshop Report 95*. MIT Press, Cambridge, MA, USA.
- Harris, L.B., Cobbold, P.R., 1985. Development of conjugate shear bands during bulk simple shearing. *Journal of Structural Geology* 7 (1), 37–44.
- Herwegh, M., Handy, M.R., 1996. The evolution of high-temperature mylonitic microfabrics: evidence from simple shearing of a quartz analogue (norcamphor). *Journal of Structural Geology* 18 (5), 689–710.
- Herwegh, M., Handy, M.R., 1998. The origin of shape preferred orientations in mylonite: inferences from in-situ experiments on polycrystalline norcamphor. *Journal of Structural Geology* 20 (6), 681–694.

- Hobbs, B.E., Ord, A., Teyssier, C., 1986. Earthquakes in the ductile regime. *Pure and Applied Geophysics* 124 (1–2), 309–336.
- Hobbs, B.E., Mühlhaus, H.-B., Ord, A., 1990. Instability, softening and localization of deformation. In: Knipe, R.J., Rutter, E.H. (Eds.), *Deformation Mechanisms, Rheology and Tectonics Geological Society Special Publications* 54, pp. 143–165.
- Hoepfner, R., 1955. Tektonik im Schiefergebirge. *Geologische Rundschau* 44, 26–58.
- Huddleston, P., 1999. Strain compatibility and shear zones: is there a problem? *Journal of Structural Geology* 21, 923–932.
- Imber, J., Holdsworth, R.E., Butler, C.A., 2001. A reappraisal of the Sibson–Scholz fault zone model: the nature of the frictional to viscous (“brittle–ductile”) transition along a long-lived, crustal scale fault, Outer Hebrides, Scotland. *Tectonics* 20 (5), 604–624.
- Ivins, E.R., Dixon, T.H., Golombek, M.P., 1990. Extensional reactivation of an abandoned thrust: a bound in shallowing the brittle regime. *Journal of Structural Geology* 12 (3), 303–314.
- Kim, Y.S., Peacock, D.C.P., Sanderson, D.J., 2004. Fault damage zones. *Journal of Structural Geology* 26 (3), 503–517.
- Lafrance, B., John, B.E., Frost, B.R., 1998. Ultra high-temperature and subsolidus shear zones: examples from the Poe Mountain orthonosite, Wyoming. *Journal of Structural Geology* 20 (7), 945–955.
- Mauffret, A., de Grossouvre, B.D., Dos Reis, A.T., Gorini, C., Nercessian, A., 2001. Structural geometry in the eastern Pyrenees and western Gulf of Lion (Western Mediterranean). *Journal of Structural Geology* 23, 1701–1726.
- Mitra, G., 1979. Ductile deformation zones in blue ridge basement rocks and estimation of finite strains. *Geological Society of America Bulletin* 90 (10), 935–951.
- Passchier, C.W., 1984. The generation of ductile and brittle shear bands in a low-angle mylonite zone. *Journal of Structural Geology* 6 (3), 273–281.
- Passchier, C.W., 2001. Flanking structures. *Journal of Structural Geology* 23 (6–7), 951–962.
- Ramsay, J.G., Graham, R.H., 1970. Strain variation in shear belts. *Canadian Journal of Earth Sciences* 7 (3), 786–813.
- Ramsay, J.G., Huber, M.L., 1983. *The Techniques of Modern Structural Geology*. Vol. 1, Strain Analysis. Academic Press, London.
- Ranalli, G., Yin, Z.-M., 1990. Critical stress difference and orientation of faults in rocks with strength anisotropies: the two-dimensional case. *Journal of Structural Geology* 12, 1067–1071.
- Regenauer-Lieb, K., Yuen, D.A., 2003. Modeling shear zones in geological and planetary sciences: solid- and fluid-thermal-mechanical approaches. *Earth-Science Reviews* 63 (3–4), 295–349.
- Rutter, E.H., 1986. On the nomenclature of mode of failure transitions in rocks. *Tectonophysics* 122 (3–4), 381–387.
- Schmid, S.M., Handy, M.R., 1991. Towards a genetic classification of fault rocks: geological usage and tectonophysical implications. In: Muller, D.W., McKenzie, J.A., Weissert, H. (Eds.), *Controversies in Modern Geology: Evolution of Geological Theories in Sedimentology, Earth History and Tectonics*. Academic Press, London, pp. 339–361.
- Scholz, C.H., 1988. The brittle–plastic transition and the depth of seismic faulting. *Geologische Rundschau* 77 (1), 319–328.
- Sibson, R.H., 1980. Transient discontinuities in ductile shear zones. *Journal of Structural Geology* 2 (1–2), 165–171.
- Stewart, M., Holdsworth, R.E., Strachan, R.A., 2000. Deformation processes and weakening mechanisms within the frictional–viscous transition zone of major crustal-scale faults: insights from the Great Glen Fault Zone, Scotland. *Journal of Structural Geology* 22, 543–560.
- Stipp, M., Stunitz, H., Heilbronner, R., Schmid, S.M., 2002. The eastern Tonale fault zone: a ‘natural laboratory’ for crystal plastic deformation of quartz over a temperature range from 250 to 700 °C. *Journal of Structural Geology* 24 (12), 1861–1884.
- Thatcher, W., England, P.C., 1998. Ductile shear zones beneath strike-slip faults: implications for the thermomechanics of the San Andreas fault zone. *Journal of Geophysical Research—Solid Earth* 103 (B1), 891–905.
- Tullis, J., Yund, R.A., 1991. Diffusion creep in feldspar aggregates—experimental evidence. *Journal of Structural Geology* 13 (9), 987–1000.
- Vermilye, J.M., Scholz, C.H., 1999. Fault propagation and segmentation: insight from the microstructural examination of a small fault. *Journal of Structural Geology* 21, 1623–1636.
- Williams, P.F., Price, G.P., 1990. Origin of kinkbands and shear-band cleavage in shear zones—an experimental study. *Journal of Structural Geology* 12 (2), 145–164.
- Yin, Z.-M., Ranalli, G., 1992. Critical stress difference, fault orientation and slip direction in anisotropic rocks under non-Andersonian stress systems. *Journal of Structural Geology* 14 (2), 237–244.